Available online at www.sciencedirect.com
SCIENCE DIRECT®
Journal of Sound and Vibration 279 (2005) 1015–1036
JOURNAL OF SOUND AND VIBRATION
www.elsevier.com/locate/jsvi

Karhunen–Loève decomposition of coupled axial/bending vibrations of beams subject to impacts

M.A. Trindade, C. Wolter, R. Sampaio*

Department of Mechanical Engineering, Pontifícia Universidade Católica do Rio de Janeiro, rua Marquês de São Vicente, 225, 22453-900 Rio de Janeiro, Brazil

Received 15 March 2002; accepted 25 November 2003

Abstract

This work presents a study of the oscillations of a vertical slender beam, clamped in its upper extreme, pinned in its lower one and constrained inside an outer cylinder in its lower portion. The beam is subject to distributed axial loads, due to its own weight, leading to geometric softening of its lower portion and thus yielding a large number of vibroimpacts with the outer cylinder. This is due to the axial–bending coupling, often called geometric stiffening and largely discussed in the last two decades. Here, it is accounted for by using a non-linear finite element model proposed in a previous work, in which non-linear strain–displacement relations are considered. To help understand this non-linear coupled vibro-impact problem, the Karhunen–Loève decomposition, also known as the proper orthogonal decomposition, is applied to its simulated dynamics. The results show that the micro-impacts, accompanying the beam–hole impacts and mainly due to the beam compressive softening, and the reaction forces at the top and bottom positions, are well represented only when using a non-linear axial–bending coupling. It is also shown that 15 proper orthogonal modes are sufficient to reconstruct the dynamics of the impacting beam under a 3% error margin.

1. Introduction

It is well-known that flexible beams subject to axial loads present strong stiffness variations. This is due to what is often called *geometric stiffening effect* in the literature [1]. It may also be seen as a consequence of the coupling between axial and bending strains. In the last two decades, several methodologies have been proposed to account for the geometric stiffening effect. In particular, Simo and Vu-Quoc [2] showed that modelling beams under large rotations using linear

*Corresponding author.
E-mail address: rsampaio@mec.puc-rio.br (R. Sampaio).

0022-460X/$ - see front matter © 2004 Elsevier Ltd. All rights reserved.
doi:10.1016/j.jsv.2003.11.057

beam theories results in a spurious loss of stiffness and hence they proposed a "consistent" linearization using steady state values for the axial internal force. Kane et al. [3] proposed a methodology, that uses higher order strain measures, and applied it to the dynamics of a cantilever beam attached to a moving base under prescribed large translation and rotation. This idea was later generalized to arbitrary flexible bodies by Banerjee and Dickens [4], Wallrapp and Schwertassek [5], and more recently by Urruzola et al. [6], to treat structural elements other than beams. Some of these models were summarized and compared by Trindade and Sampaio [7] using a general non-linear model, resulting from non-linear strain–displacement relations. Their conclusion is that a non-linear model accounting for the coupling between axial and bending vibrations is required for an accurate representation of the dynamics of slender beams.

Due to the non-linearity induced by the geometric stiffening, augmented by the intrinsic non-linear behavior of vibroimpacting structures, one is obliged to consider non-linear analysis techniques. The Karhunen–Loève (KL) decomposition, also known as the proper orthogonal decomposition, is a powerful tool for obtaining spatial information and providing a basis for model reduction of non-linear structural systems [8–10]. It consists in obtaining a set of orthogonal eigenfunctions (or proper orthogonal modes) where the dynamics is to be projected. This set of KL modes are optimal in the sense that it minimizes the error of the approximation for any number of modes considered, meaning that no other linear expansion may lead to a better representation of the dynamics response with the same number of modes. Indeed, Steindl and Troger [10] concluded, in their comparative work, that KL modes are by far the best choice for a standard Galerkin approximation. Practically, the KL decomposition is obtained by constructing a spatial autocorrelation tensor from the simulated or measured dynamics of the system. Thereafter, performing its spectral decomposition, one finds that the spatial autocorrelation tensor eigenfunctions provide the required proper orthogonal modes and its eigenvalues represent the mean energy contained in that projection. This technique was previously used for the analysis of vibroimpact problems by Azeez and Vakakis [9] and Wolter and Sampaio [11]. Other model reduction techniques applied for a similar vibroimpact problem were also presented by Friswell et al. [12].

In the present work, the non-linear oscillations of a typical configuration of drillstring used for oilwell drilling are studied. Drillstring dynamics can present complex vibrational states and there is a strong need to understand it in order to better control the drilling process. Several works on drillstring dynamics have been published in the literature. Yigit and Christoforou [13] developed a model to study the transverse vibrations of drillstrings caused by axial loading and impact with the wellbore wall. In a later work, the same authors extended their model to account also for torsional vibrations [14]. Tucker and Wang [15] have presented more recently an integrated model for drillstring dynamics accounting for axial, bending and torsional vibrations.

Here, the drillstring is represented by a vertical slender beam, clamped in its upper extreme, pinned in its lower one and constrained inside an outer cylinder in its lower portion. The beam is subject to distributed axial loads, due to its own weight, leading to geometric softening of its lower portion and thus yielding a large number of vibroimpacts with the outer cylinder. To help understand this non-linear coupled vibroimpact problem, the KL decomposition is applied to its simulated dynamics, which is evaluated using an extension of the non-linear finite element (FE) model proposed in a previous work [7].

2. Non-linear model formulation

Let us consider an initially straight and slender cylinder, of undeformed length L and outer and inner radii R_o and R_i, undergoing large displacements and small deformations as shown in Fig. 1.

2.1. Displacements and strain measures

Small deformations are assumed so that the beam cross-section rotation angle β is small. Also, the assumption of negligible shear strains, leading to $\beta = -v'$, is considered. Notice that the prime denotes the derivative with respect to the axial co-ordinate x. Consequently, the displacement vector $\mathbf{p}$ of a given point with position $\mathbf{X}$ in the xz plane is

$$\mathbf{p} = \begin{Bmatrix} u - zv' \\ v \end{Bmatrix} \quad \text{for } \mathbf{X} = \begin{Bmatrix} x \\ z \end{Bmatrix}, \tag{1}$$

where x and z directions are such that $0 \leqslant x \leqslant L$ and $-R_o \leqslant z \leqslant R_o$. The deformation gradient $\mathbf{F}$ relative to the reference position is defined as

$$\mathbf{F} = \left(\frac{\mathrm{d}\mathbf{p}}{\mathrm{d}\mathbf{X}} + \mathbf{I} \right) \tag{2}$$

with $\mathbf{I}$ defining the identity operator. The Lagrangian strain tensor $\mathbf{E}$ reads

$$\mathbf{E} = \tfrac{1}{2}(\mathbf{F}^{\mathrm{T}}\mathbf{F} - \mathbf{I}) = \frac{1}{2}\left[\left(\frac{\mathrm{d}\mathbf{p}}{\mathrm{d}\mathbf{X}} \right) + \left(\frac{\mathrm{d}\mathbf{p}}{\mathrm{d}\mathbf{X}} \right)^{\mathrm{T}} + \left(\frac{\mathrm{d}\mathbf{p}}{\mathrm{d}\mathbf{X}} \right)^{\mathrm{T}} \left(\frac{\mathrm{d}\mathbf{p}}{\mathrm{d}\mathbf{X}} \right) \right]. \tag{3}$$

Here, only the axial component of the strain tensor $\varepsilon_{xx} \equiv E_{11}$ is considered. Therefore, defining the axial displacement as $u_0 = u - zv'$, the non-linear axial strain ε_{xx} may be written in the form

$$\varepsilon_{xx} = u_0' + \tfrac{1}{2}[(u_0')^2 + (v')^2]. \tag{4}$$

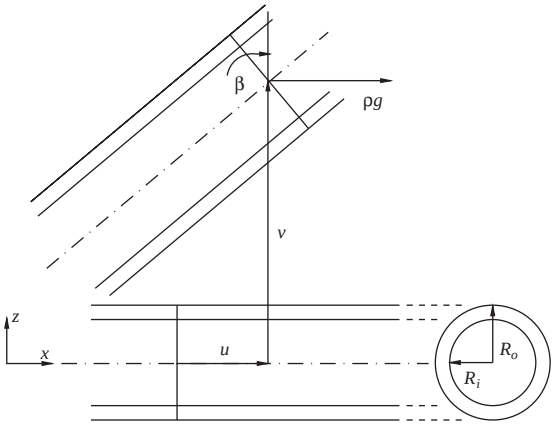

Fig. 1. Slender cylinder undergoing large displacements and small deformations.

2.2. Strain and kinetic energies

From the assumption of negligible shear strains and also neglecting the contribution of transversal normal stress σ_{zz}, the strain potential energy of the beam is

$$H = \frac{1}{2}\int E\varepsilon_{xx}^2 \,\mathrm{d}V, \tag{5}$$

where E is the Young's modulus of the beam. Considering a symmetric beam cross-section with respect to z-axis and using the axial strain definition (4), the potential energy (5) of the beam may be written in terms of the mean axial u and transversal v displacements only. Thus,

$$H = \frac{1}{2}\int_0^L \left[EA\left(u'^2 + \underline{u'v'^2 + (1/4)v'^4} + \underline{\underline{u'^3 + (1/4)u'^4}} + \underline{\underline{(1/2)u'^2v'^2}} \right) + EI\left(v''^2 + \underline{\underline{3u'v''^2 + (3/2)u'^2v''^2 + (3h^2/20)v''^4}} + \underline{\underline{(1/2)v'^2v''^2}} \right) \right] \mathrm{d}x, \tag{6}$$

where A and I are the area and moment of inertia of the beam cross-section and h is its thickness. Single underlined terms in Eq. (6) are due to the presence of term $(v')^2$, quadratic in the cross-section rotation angle $\beta = -v'$, in the axial strain ε_{xx}. Notice that they appear only in the membrane strain component, unlike double and triple underlined terms that are present in both membrane and bending components of the strain energy. The term $(u_0')^2$, quadratic in the axial displacement derivative, in the axial strain (4) leads to the double underlined terms in the strain energy function, while triple underlined terms are due to the coupling between the two quadratic terms of the axial strain. It is worthwhile to notice also that the assumption of a linear strain–displacement relation eliminates all underlined terms of Eq. (6).

In the present work, only the contributions of cubic and lower order terms in u_0' and v' are retained in the potential energy (6). From the definition of u_0, this leads to the simplified potential energy

$$H_s = \frac{1}{2}\int_0^L \left[EA\left(u'^2 + \underline{u'v'^2} + \underline{\underline{u'^3}} \right) + EI\left(v''^2 + \underline{\underline{3u'v''^2}} \right) \right] \mathrm{d}x. \tag{7}$$

The kinetic energy of the beam may also be written in terms of the main variables u and v. Hence, starting from the general form of the kinetic energy in terms of the total displacement of the beam, one gets

$$T = \frac{1}{2}\int \rho \dot{\mathbf{p}}^{\mathrm{T}}\dot{\mathbf{p}} \,\mathrm{d}V, \tag{8}$$

where ρ is the beam mass density and $\dot{\mathbf{p}}$ is the velocity vector of a given point $\mathbf{X}$ of the beam. From Eq. (1), defining $\mathbf{p}$, and assuming a symmetric beam cross-section with respect to z-axis, the kinetic energy of the beam may be written in terms of the main variables u and v as

$$T = \frac{1}{2}\int_0^L [\rho A(\dot{u}^2 + \dot{v}^2) + \rho I\dot{v}'^2] \,\mathrm{d}x, \tag{9}$$

where the terms in Eq. (9) correspond to inertia contributions due to translation, in x and z directions, and cross-section rotation.

The beam is subject to its own weight, which may be expressed as the following vertical forces, that is in the x direction, due to the gravity field:

$$\mathbf{f}_g = \begin{Bmatrix} \rho g \\ 0 \end{Bmatrix} \tag{10}$$

and, assuming symmetric cross-section, their work may be written as

$$W = \int \mathbf{p}^{\mathrm{T}} \mathbf{f}_g \, \mathrm{d}V = \int_0^L \rho g A u \, \mathrm{d}x. \tag{11}$$

2.3. Variational formulation

Using the expressions for strain (Eq. (7)) and kinetic (Eq. (9)) energies and work due to gravity forces (Eq. (11)) presented above, a variational formulation is used in this section to derive the FE model.

The virtual variation of the simplified strain energy H_s is decomposed in linear and non-linear contributions arising from the non-linear strain–displacement relations (4) and, hence, is written as

$$\delta H_s = \delta H_{sl} + \delta H_{sn}, \tag{12}$$

where the linear δH_{sl} and non-linear δH_{sn} contributions are expressed in terms of the variations $\delta u'$, $\delta v'$ and $\delta v''$ as

$$\delta H_{sl} = \int_0^L (\delta u' EA u' + \delta v'' EI v'') \, \mathrm{d}x, \tag{13}$$

$$\delta H_{sn} = \int_0^L \left[\tfrac{1}{2} \delta u' EA(3u'^2 + v'^2) + \tfrac{3}{2} \delta u' EI v''^2 + 3\delta v'' EI u' v'' + \delta v' EA u' v' \right] \mathrm{d}x. \tag{14}$$

Notice that the non-linear contributions δH_{sn} come from the underlined terms in Eq. (7). On the other hand, the linear contributions δH_{sl} are the standard ones for Euler–Bernoulli beams.

The virtual variation of the kinetic energy T may be derived from Eq. (9), leading to

$$\delta T = \int_0^L [\rho A(\delta \dot{u}\dot{u} + \delta \dot{v}\dot{v}) + \rho I \delta \dot{v}' \dot{v}'] \, \mathrm{d}x, \tag{15}$$

which through integration in time is equivalent to

$$\int_{t_1}^{t_2} \delta T = -\int_{t_1}^{t_2} \int_0^L [\rho A(\delta u \ddot{u} + \delta v \ddot{v}) + \rho I \delta v' \ddot{v}'] \, \mathrm{d}x. \tag{16}$$

This expression may also be interpreted as the virtual work done by the inertial forces, composed of translation in x and z directions and cross-section rotation in the xz plane.

The virtual work done by the gravity forces is obtained from Eq. (11) and is written in terms of δu only since these forces keep their vertical x direction under deformation:

$$\delta W = \int_0^L \rho g A \delta u \, \mathrm{d}x. \tag{17}$$

2.4. Non-linear FE model

The FE model is constructed through discretization of the virtual variations of strain (Eq. (12)) and kinetic (Eq. (16)) energies. It is clear that neglecting the other terms in the strain energy (Eq. (6)) leads to the absence of several non-linear terms in the model. However, it is assumed for now that the main contributions to the axial–bending coupling should be accounted for by the terms considered in Eq. (7).

The discretization is carried out using Lagrange linear shape functions for the axial displacement u and Hermite cubic ones for the transversal deflection v. This leads to an element with six degrees of freedom $\mathbf{q}_e^{\mathrm{T}} = \{u_1 \; v_1 \; \beta_1 \; u_2 \; v_2 \; \beta_2\}$, where $(\beta_1, \beta_2) = (v_1', v_2')$. Moreover, the axial and transversal displacements are discretized as

$$u = \mathbf{N}_u \mathbf{q}_e, \quad v = \mathbf{N}_v \mathbf{q}_e, \tag{18}$$

where, defining the element length ℓ and the adimensional axial position $\xi = x/\ell$,

$$\begin{aligned} \mathbf{N}_u &= \{\, 1-\xi \quad 0 \quad 0 \quad \xi \quad 0 \quad 0 \,\}, \\ \mathbf{N}_v &= \left\{ 0 \quad 1-3\xi^2+2\xi^3 \quad \xi\ell(1-\xi)^2 \quad 0 \quad \xi^2(3-2\xi) \quad \xi^2\ell(\xi-1) \right\}. \end{aligned} \tag{19}$$

Replacing the discrete expressions for the displacements and their derivatives in the elementary versions of linear and non-linear contributions to the virtual variation of strain energy, Eqs. (13) and (14), leads to

$$\delta H_{sl}^e = \delta \mathbf{q}_e^{\mathrm{T}} \mathbf{K}_e^e \mathbf{q}_e, \quad \delta H_{sn}^e = \delta \mathbf{q}_e^{\mathrm{T}} \mathbf{K}_g^e \mathbf{q}_e, \tag{20}$$

where the expressions for the elementary linear elastic stiffness $\mathbf{K}_e^e$ and non-linear geometric stiffness $\mathbf{K}_g^e$ matrices are

$$\mathbf{K}_e^e = \int_0^\ell (EA \mathbf{N}_u'^{\mathrm{T}} \mathbf{N}_u' + EI \mathbf{N}_v''^{\mathrm{T}} \mathbf{N}_v'') \, \mathrm{d}x, \tag{21}$$

$$\begin{aligned} \mathbf{K}_g^e = \int_0^\ell \big[& EA \left(\tfrac{3}{2} \mathbf{N}_u'^{\mathrm{T}} \mathbf{N}_u' \mathbf{q}_e \mathbf{N}_u' + \tfrac{1}{2} \mathbf{N}_u'^{\mathrm{T}} \mathbf{N}_v' \mathbf{q}_e \mathbf{N}_v' + \mathbf{N}_v'^{\mathrm{T}} \mathbf{N}_u' \mathbf{q}_e \mathbf{N}_v' \right) \\ & + EI \left(\tfrac{3}{2} \mathbf{N}_u'^{\mathrm{T}} \mathbf{N}_v'' \mathbf{q}_e \mathbf{N}_v'' + 3 \mathbf{N}_v''^{\mathrm{T}} \mathbf{N}_u' \mathbf{q}_e \mathbf{N}_v'' \right) \big] \, \mathrm{d}x. \end{aligned} \tag{22}$$

The mass matrix is obtained from the discretization of the inertial forces virtual work, Eq. (16). Hence, replacing the discrete expressions of the displacements in Eq. (16) leads to

$$\int_{t_1}^{t_2} \delta T^e \, \mathrm{d}t = - \int_{t_1}^{t_2} \delta \mathbf{q}_e^{\mathrm{T}} \mathbf{M}^e \ddot{\mathbf{q}}_e \, \mathrm{d}t, \tag{23}$$

where the elementary mass matrix $\mathbf{M}^e$ is

$$\mathbf{M}^e = \int_0^\ell (\rho A \mathbf{N}_u^{\mathrm{T}} \mathbf{N}_u + \rho A \mathbf{N}_v^{\mathrm{T}} \mathbf{N}_v + \rho I \mathbf{N}_v'^{\mathrm{T}} \mathbf{N}_v') \, \mathrm{d}x. \tag{24}$$

The elementary virtual work done by the gravity forces is also discretized using the discrete expression of the axial displacement yielding

$$\delta W^e = \delta \mathbf{q}_e^{\mathrm{T}} \mathbf{F}_g^e, \tag{25}$$

where the elementary load vector resulting from the gravity field is

$$\mathbf{F}_g^e = \int_0^\ell \rho g A \mathbf{N}_u^{\mathrm{T}} \, \mathrm{d}x. \tag{26}$$

Therefore, the discretized virtual variations may be introduced in Hamilton's principle,

$$\delta \int_{t_1}^{t_2} (T - H_s + W) \, \mathrm{d}t = 0, \tag{27}$$

which, from Eqs. (20), (23) and (25) and after assembling all elements, yields the following discretized equations of motion:

$$\mathbf{M}\ddot{\mathbf{q}} + [\mathbf{K}_e + \mathbf{K}_g(\mathbf{q})]\mathbf{q} = \mathbf{F}_g, \tag{28}$$

where $\ddot{\mathbf{q}}$ defines the acceleration vector. Point forces and damping matrices can be imposed a posteriori on the system. The element mass matrix (24) may be decomposed in translation $\mathbf{M}_{tr}^e$ and rotation $\mathbf{M}_{rot}^e$ contributions which are

$$\mathbf{M}_{tr}^e = \frac{\rho A \ell}{420} \begin{bmatrix} 140 & 0 & 0 & 70 & 0 & 0 \\ & 156 & 22\ell & 0 & 54 & -13\ell \\ & & 4\ell^2 & 0 & 13\ell & -3\ell^2 \\ & & & 140 & 0 & 0 \\ & sym & & & 156 & -22\ell \\ & & & & & 4\ell^2 \end{bmatrix},$$

$$\mathbf{M}_{rot}^e = \frac{\rho I}{\ell} \begin{bmatrix} 0 & 0 & 0 & 0 & 0 & 0 \\ & 6/5 & 1/10\ell & 0 & -6/5 & 1/10\ell \\ & & 2/15\ell^2 & 0 & -1/10\ell & -1/30\ell^2 \\ & & & 0 & 0 & 0 \\ & sym & & & 6/5 & -1/10\ell \\ & & & & & 2/15\ell^2 \end{bmatrix}. \tag{29}$$

The symmetric linear elastic stiffness matrix $\mathbf{K}_e^e$ corresponds to that of standard Euler–Bernoulli beams with axial and bending stiffnesses. $\mathbf{K}_g^e$ states for the geometric stiffness which, as presented previously, depends on the configuration and thus corresponds to the non-linear terms in the

equations of motion. These stiffness matrices are

$$\mathbf{K}_e^e = \frac{E}{\ell}\begin{bmatrix} A & 0 & 0 & -A & 0 & 0 \\ & 12I/\ell^2 & 6I/\ell & 0 & -12I/\ell^2 & 6I/\ell \\ & & 4I & 0 & -6I/\ell & 2I \\ & & & A & 0 & 0 \\ & sym & & & 12I/\ell^2 & -6I/\ell \\ & & & & & 4I \end{bmatrix}, \tag{30}$$

$$\mathbf{K}_g^e = \frac{EA}{60\ell^2}\begin{bmatrix} 90\tilde{u} & -3(1+3r)(\ell\bar{\beta}-12\tilde{v}) & \ell(1+3r)(-4\ell\bar{\beta}+5\beta_2\ell+3\tilde{v}) \\ 0 & 72\tilde{u}(1+3r) & 6\ell\tilde{u}(1+3r) \\ 0 & 6\ell\tilde{u}(1+3r) & 8\ell^2\tilde{u}(1+3r) \\ -90\tilde{u} & 3(1+3r)(\ell\bar{\beta}-12\tilde{v}) & -\ell(1+3r)(-4\ell\bar{\beta}+5\beta_2\ell+3\tilde{v}) \\ 0 & -72\tilde{u}(1+3r) & -6\ell\tilde{u}(1+3r) \\ 0 & 6\ell\tilde{u}(1+3r) & -2\ell^2\tilde{u}(1+3r) \end{bmatrix}$$

$$\begin{bmatrix} -90\tilde{u} & 3(1+3r)(\ell\bar{\beta}-12\tilde{v}) & -\ell(1+3r)(-\ell\bar{\beta}+5\beta_2\ell-3\tilde{v}) \\ 0 & -72\tilde{u}(1+3r) & 6\ell\tilde{u}(1+3r) \\ 0 & -6\ell\tilde{u}(1+3r) & -2\ell^2\tilde{u}(1+3r) \\ 90\tilde{u} & -3(1+3r)(\ell\bar{\beta}-12\tilde{v}) & \ell(1+3r)(-\ell\bar{\beta}+5\beta_2\ell-3\tilde{v}) \\ 0 & 72\tilde{u}(1+3r) & -6\ell\tilde{u}(1+3r) \\ 0 & -6\ell\tilde{u}(1+3r) & 8\ell^2\tilde{u}(1+3r) \end{bmatrix}, \tag{31}$$

where $r = I/A$. Notice that the geometric stiffness matrix $\mathbf{K}_g^e$ depends on the variables $\tilde{u} = u_2 - u_1$, $\tilde{v} = v_2 - v_1$ and $\bar{\beta} = \beta_1 + \beta_2$. Moreover, the bending stiffness $2/15(1+3r)EA\tilde{u}$ varies linearly with the relative axial displacement $\tilde{u}$. That is, this stiffness increases when $\tilde{u}$ is positive and decreases in the opposite case. This is in agreement with the notion that the beam is stiffer in bending when under extension and, on the contrary, it is less stiff when under axial compression.

2.5. Accounting for initial deformed configuration

In this section, the non-linear FE model is applied to a typical configuration of drillstring used for oilwell drilling, which can be represented by a vertical slender cylinder clamped at its top position, axially sliding at its bottom position and subject to its own weight. Hence, the boundary conditions considered here are: all degrees of freedom locked at the top position and transversal displacement locked at the bottom position. Fig. 2 presents the idealized undeformed and deformed configurations for the drillstring. Three a posteriori forces are now introduced in the FE

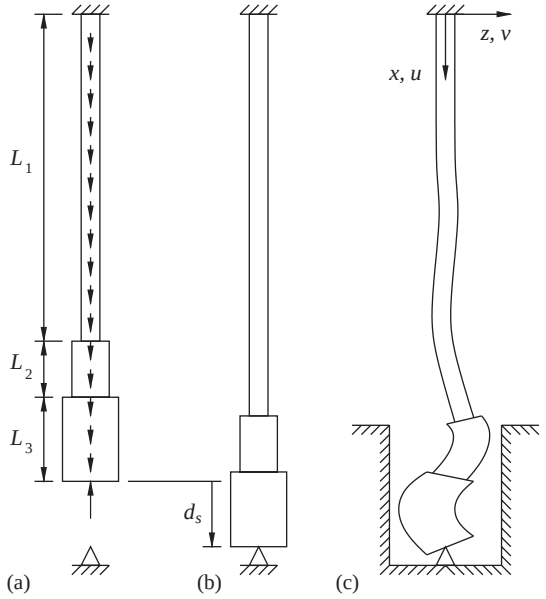

Fig. 2. (a) Undeformed, (b) initial deformed and (c) deformed configurations for a typical drillstring.

model. In addition to the constant gravity forces, an also constant negative axial point force, represented by the force vector $\mathbf{F}_f$, is applied at the beam free end, the drill bit, to simulate the static reaction force when the bit touches the formation. Notice that the gravity force $\mathbf{F}_g$ and the reaction force $\mathbf{F}_f$ are time-invariant. Two external forces are also applied to the drillstring, namely a contact force $\mathbf{F}_c$ due to the beam–hole impacts (Fig. 2(c)) and a perturbation force $\mathbf{F}_p$ due to induced vibrations. Therefore, the equations of motion (28) may be rewritten as

$$\mathbf{M}\ddot{\mathbf{q}} + [\mathbf{K}_e + \mathbf{K}_g(\mathbf{q})]\mathbf{q} = \mathbf{F}_g - \mathbf{F}_f + \mathbf{F}_c + \mathbf{F}_p. \tag{32}$$

In the practical case, the drillstring is lowered until the drill bit touches the formation. In the event of continued lowering, the reaction force of the formation $\mathbf{F}_f$, applied to the drill bit, grows and the lower part of the drillstring is compressed. In the present work, it is supposed that after this quasi-static lowering and when the reaction force reaches a given value, the axial displacement of the drill bit is locked (Fig. 2(b)). Therefore, further motions occur around this initial deformed configuration, which is the solution of the equation

$$[\mathbf{K}_e + \mathbf{K}_g(\mathbf{q}_s)]\mathbf{q}_s = \mathbf{F}_g - \mathbf{F}_f. \tag{33}$$

This equation holds because $\mathbf{F}_c$ and $\mathbf{F}_p$ are initially zero, that is, there is neither beam–hole contact nor external perturbation.

Since the drillstring is supposed to be initially straight and only axial components of both gravity $\mathbf{F}_g$ and reaction $\mathbf{F}_f$ forces are non-null, one may expect that only the elements corresponding to axial displacements in $\mathbf{K}_g(\mathbf{q}_s)$ will not vanish (see Eq. (31)). Moreover, in this case, the elements of $\mathbf{K}_g(\mathbf{q}_s)$, e.g., $3EA\tilde{u}/2\ell^2$, are negligible compared to those of $\mathbf{K}_e$, e.g., EA/ℓ, since generally $\tilde{u} \ll \ell$. Hence, the initial static displacement vector $\mathbf{q}_s$ may be found through the

solution of the previous algebraic equation with $\mathbf{K}_g(\mathbf{q}_s) = \mathbf{0}$, leading to

$$\mathbf{q}_s = \mathbf{K}_e^{-1}(\mathbf{F}_g - \mathbf{F}_f). \tag{34}$$

This is the initial deformed configuration of the drillstring, which is represented in Fig. 2(b). Let us define then a new displacement vector $\bar{\mathbf{q}}$ relative to the static one $\mathbf{q}_s$ as

$$\bar{\mathbf{q}} = \mathbf{q} - \mathbf{q}_s. \tag{35}$$

Substituting $\mathbf{q}$ by $\bar{\mathbf{q}} + \mathbf{q}_s$ in Eq. (32) and accounting for Eq. (34), one can write a new set of equations of motion in terms of the relative displacement vector $\bar{\mathbf{q}}$,

$$\mathbf{M}\ddot{\bar{\mathbf{q}}} + [\mathbf{K}_e + \mathbf{K}_g(\bar{\mathbf{q}} + \mathbf{q}_s)]\bar{\mathbf{q}} = \mathbf{F}_c + \mathbf{F}_p. \tag{36}$$

The axial displacement of the drill bit is then locked into its static value, such that $\bar{u}^L = 0$, or $u^L = u_s^L$. The last equation then becomes

$$\mathbf{M}_r\ddot{\bar{\mathbf{q}}}_r + [\mathbf{K}_{er} + \mathbf{K}_{gr}(\bar{\mathbf{q}} + \mathbf{q}_s)]\bar{\mathbf{q}}_r = \mathbf{F}_{cr} + \mathbf{F}_{pr}, \tag{37}$$

where $\bar{\mathbf{q}}_r$ is the reduced relative displacement vector. Notice that the reduced mass and stiffness matrices are those for axial and transversal displacements locked at the bottom position (that is, a clamped–hinged beam, as shown in Fig. 2(c)). The global response is then obtained through summation of the relative displacements, augmented by the nil relative axial displacement at the bottom position $\{\bar{\mathbf{q}}_r^{\mathrm{T}}\ 0\}^{\mathrm{T}}$, with the static displacements $\mathbf{q}_s$.

The contact force vector $\mathbf{F}_c$ in Eq. (36) is composed of nodal impact forces F_c^j that depend on whether the corresponding FE node j is in contact with the borehole, and is subject to the following law:

$$F_c^j(t) = \begin{cases} 0 & \text{if } |v^j(t)| \leqslant \varepsilon, \\ -k\{|v^j(t)| - \varepsilon\ \mathrm{sign}[v^j(t)]\} & \text{if } |v^j(t)| > \varepsilon, \end{cases} \tag{38}$$

where ε is the distance between the outer surface of the drillstring and the borehole wall and v^j is the transversal displacement of the node j. One may notice from Eq. (38) that the impact force is supposed to be either linear elastic, with spring constant k when there exists beam–hole contact, or zero otherwise. One could also consider a non-linear spring and/or a damping mechanism to account for inelastic impacts, however in this work simple assumptions for the impact are made to focus attention on the geometric stiffening effects. The impact force is also supposed to have only transversal components, that is, the beam–hole friction effect is neglected. However, a modal damping of 5%, relative to the linear elastic model, was considered a posteriori to approximate all forms of damping of the system.

3. Numerical results

In the three following sections, the dynamics of a typical configuration of drillstring, studied experimentally by Sotomayor et al. [16], is simulated using the non-linear FE model presented previously and analyzed with the help of the KL decomposition. The strategy shown in the previous section to account for the initial deformation state is also used. The geometrical and material properties of the drillstring were adapted from Ref. [16] and are shown in Table 1. The drillstring is divided in three different cross-sections, as shown in Fig. 2. The upper portion, composed of drill

Table 1
Geometrical and material properties of the drillstring

	Section 1	Section 2	Section 3
Young's modulus E (GPa)	210	210	210
Mass density ρ (kg m^3)	7850	7850	7850
External radius R_o (m)	0.064	0.064	0.102
Internal radius R_i (m)	0.054	0.038	0.038
Length L (m)	1700	100	200

pipes, is normally subject to large traction forces and hence is much less flexible in bending than the rest of the drillstring; it is consequently designed with small outer diameter and thin wall. On the other hand, the lower portion, composed of drill collars, is highly compressed by the weight of the upper portion and thus is subject to higher bending effects. That is why it is designed to have a larger outer diameter and a thicker wall. As for the transition portion, denoted as the heavy weight drill pipes section, located between the drill pipes and drill collars sections, it is designed to have the outer diameter of the drill pipes and the inner diameter of the drill collars.

The lower portion of the drillstring is confined inside a borehole of radius $R_h = 0.156$ m and has two stabilizers located 25 and 50 m away from the drill bit ($x = 1975$ and $x = 1950$ m, respectively). In this work, the stabilizers are accounted for by locking the beam transversal displacements at their positions. The spring constant considered for the elastic impact forces is $k = 10^8$ N/m and the clearance ε is obtained from the difference between the radii of the borehole and drillstring sections, $\varepsilon = R_h - R_o$. As explained in the previous section, the axial displacement of the drill bit is locked into its static deformed position. This is done by considering an axial static reaction force at the bottom position of 200 KN. In addition, a sinusoidal perturbation moment of $50 \sin 2\pi t$ KN m is applied through $\mathbf{F}_p$ to the hinged bottom position to simulate bit-formation-induced lateral vibration. Since, in the present study, the axial displacements are supposed to be initially at their static values, they can be excited only through coupling with bending vibrations.

3.1. Drillstring dynamics simulation

The evolution of the axial displacement, relative to the static one, at a position 6.25 m from the drill bit ($x_m = 1993.75$ m) is shown in Fig. 3, for both linear and non-linear models. One can observe that the axial displacement is very small for the linear model (Fig. 3(a)). This is due to the fact that, in this model, axial displacement is not coupled to the transversal displacement, which is the only one excited by the perturbation force considered. Indeed, these values for the axial displacement in the linear model are believed to be due to numerical integration errors. On the other hand, it is clear from the results for the non-linear model (Fig. 3(b)) that the axial displacement is indeed excited. Although much smaller than the static axial displacement, which is the reason why it is generally neglected, the effect of the variation of axial displacement relative to the static one will be evidenced later in this work.

Fig. 4 shows the transversal displacement on the bottom portion of the drill collar ($x_m = 1993.75$ m), evaluated through integration in time of the linear (Fig. 4(a)) and non-linear (Fig. 4(b)) equations of motion. The bottom portion–hole clearance is also shown in the figure, by

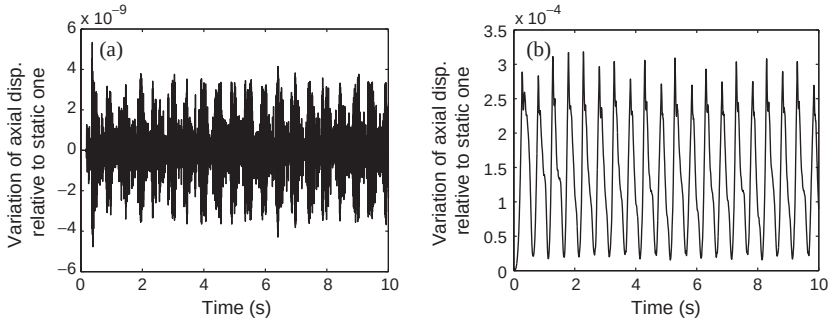

Fig. 3. Variation of axial displacement relative to the static one $u^m(t)/u_s^m$ at a position 6.25 m from the drill bit ($x_m = 1993.75$ m) using (a) linear and (b) non-linear models.

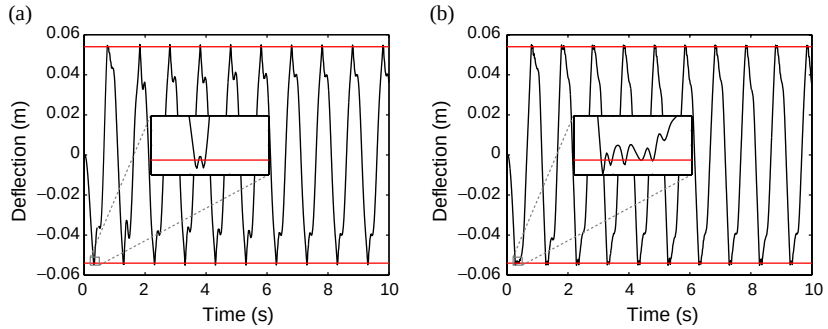

Fig. 4. Transversal displacement at a position 6.25 m from the drill bit ($x_m = 1993.75$ m) using (a) linear and (b) non-linear models.

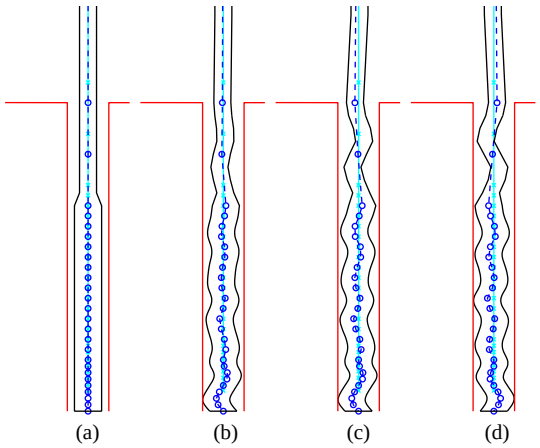

Fig. 5. Deformed configurations at integration times: (a) 0, (b) 3.5, (c) 6.5 and (d) 10 s (not in scale, drawing window for each instant 0.936 m × 395 m); ×, undeformed FE nodal points; ◦, deformed FE nodal points.

which one can notice that the drill collar is continuously under impact with the borehole wall. This is in part due to the excitation at the drill bit and in part due to the extra bending flexibility caused by the compression of the lower portion of the drillstring. To improve clarity, the first impact instant is also shown in detail for linear and non-linear models. A comparison between Figs. 4(a) and (b) shows that the non-linear model leads to a larger number of micro-impacts than the linear one. This is probably due to the higher flexibility in bending of this portion of the drillstring, caused by the axial–bending coupling, only accounted for in the non-linear model.

The deformed configurations of the drillstring bottom portion at four different integration times, 0, 3.5, 6.5 and 10 s, are represented in Fig. 5. Notice that they are not in scale to facilitate the observation of the drillstring bottom portion bending vibrations and the impacts with the borehole at multiple locations of the drill collars section. As expected, most of the bending vibration is concentrated in the bottom portion of the drillstring, that is, in the heavy weight drill pipes and drill collars. That is why the upper portion of the drillstring is not shown in Fig. 5. It is also possible to observe in this figure, the static axial displacement (at $t = 0$ s) compared to the undeformed configuration, represented by the $\times$ symbols.

The effect of non-linear coupling between axial and transversal vibrations is specially evidenced in the following analysis of the reaction forces. Fig. 6 shows the reaction forces at the top and bottom positions using linear (Fig. 6(a,b)) and non-linear (Fig. 6(c,d)) models. Comparison between Figs. 6(a) and (c) shows that the linear model, for which axial and transversal vibrations are uncoupled, is unable to capture the vibrations transmitted to the rotary table (at the top position, where the drillstring is clamped). Only the static force, due to the drillstring weight, is well represented by the linear model. On the contrary, the non-linear model is able to capture the variation of the force at the top position compared to its static value, though it is small, as shown

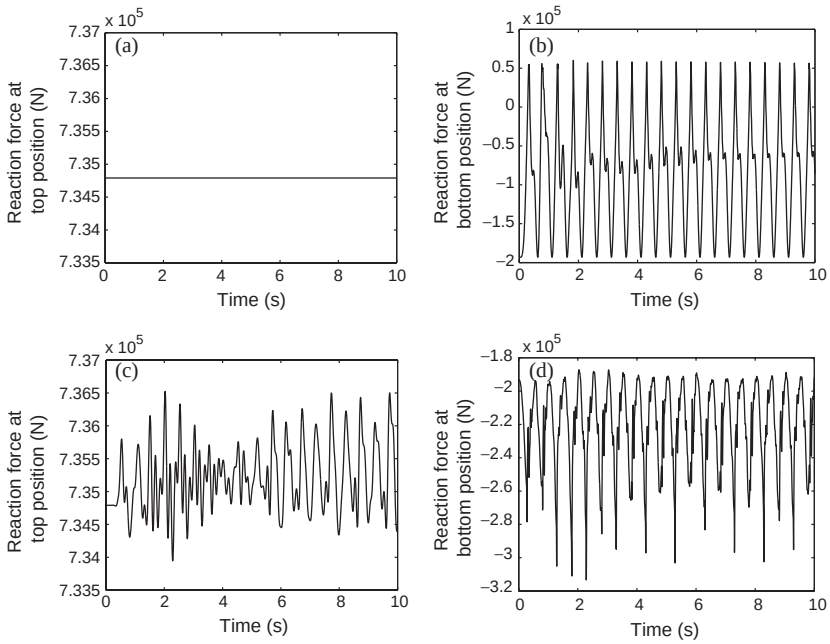

Fig. 6. Reaction forces at the top and bottom positions using (a,b) linear and (c,d) non-linear models.

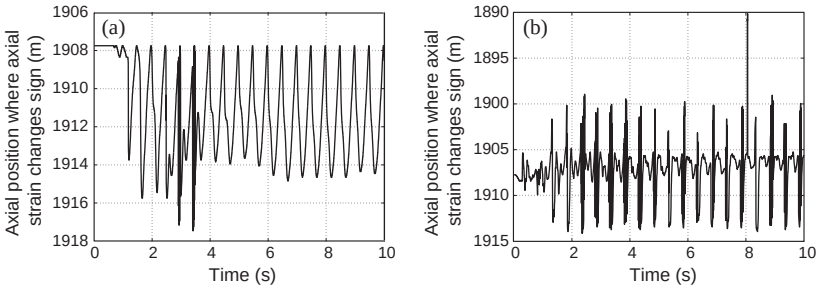

Fig. 7. Position where the axial strain changes sign using (a) linear and (b) non-linear models.

in Fig. 6(c). However, the results for the reaction forces at the bottom position using the linear and non-linear models present larger and more important differences. From Fig. 6(b), one concludes that the linear model allows the reaction force at the bottom position to be positive. This means that the drill bit is pulled from the bottom position, making it possible for the drill bit to loose contact with the formation for the larger values of deflection. This is clearly prevented here, since the axial displacement of the drill bit is locked at its static value. Nevertheless, the decrease in the force magnitude leads to a worse drilling performance. On the other hand, analysis of Fig. 6(d) shows that this behavior is not observed, for the present case, when using the non-linear model. It is thus only a consequence of neglecting the coupling between axial and bending strains. In fact, the use of the non-linear model leads to an increase in the force magnitude due to lateral vibration. This may be explained by the fact that the transversal displacement induces an increase in the axial displacement, leading to an augmentation of the compression in the bottom portion of the drill collars section, instead of inducing its traction. Notice that this effect of counterbalance between compression and traction may vary according to the parameters of the drillstring and to the static value of reaction force.

Another interesting analysis stems from the evaluation of the axial position in the drillstring that separates its compressed (lower) and stretched (upper) portions. This position is quite important in practice, since it should always lie inside the stiffer region of the drillstring, generally in the drill collars section, to prevent buckling. Therefore, Fig. 7 shows the evolution of this position in time due to the perturbation-induced vibrations, using linear and non-linear models. Due to the parameters chosen here, the static value of this position is somewhere near the center of the drill collars section. For the linear model, this position oscillates between its static value and 10 m below it (Fig. 7(a)). This means that larger portions of the drill collars section become stretched. For the non-linear model, however, this position is oscillating about its static value in a range of 15 m (Fig. 7(b)).

3.2. Karhunen–Loève decomposition of the response

In this section, the direct method of Karhunen–Loève decomposition [11,17] is applied to the drillstring dynamics. For this purpose, the time response $\mathbf{q}(t)$ is subtracted from its mean $E[\mathbf{q}(t)]$ to obtain the deviation $\mathbf{q}_d(t) = \mathbf{q}(t) - E[\mathbf{q}(t)]$ of the time response. Consequently, the new vector $\mathbf{q}_d(t)$ has elements with zero mean. As the time response $\mathbf{q}(t)$, and thus also $\mathbf{q}_d(t)$, results from time integration of the discretized equations of motion (37), it is in fact sampled in M instants of time $t_1, t_2, \ldots, t_M$, chosen in the time integration algorithm. Hence, the time response $\mathbf{q}(t)$ may be

written as a sampling matrix of dimension $M \times N$,

$$\mathbf{q} = \begin{bmatrix} q_1(t_1) & q_2(t_1) & \dots & q_N(t_1) \\ q_1(t_2) & q_2(t_2) & \dots & q_N(t_2) \\ \vdots & \vdots & \ddots & \vdots \\ q_1(t_M) & q_2(t_M) & \dots & q_N(t_M) \end{bmatrix}, \tag{39}$$

where each column represents the time response of a given degree of freedom from the FE mesh, with N being the total number of degrees of freedom or the dimension of $\mathbf{q}(t)$. Alternatively, each row represents the spatial distribution of the response at a given time instant, that is, a point in the N-dimensional phase space.

Using the ergodicity assumption, the mean value $E[\mathbf{q}(t)]$ may be obtained by the time average of $\mathbf{q}$, that is $\sum_i^M \mathbf{q}(t_i)/M$. Hence, the deviation $\mathbf{q}_d(t)$ with respect to the mean may also be written as a sampling matrix, obtained by subtracting from each line of $\mathbf{q}$ the time average of all rows,

$$\mathbf{q}_d = \mathbf{q} - \mathbf{q}_E; \quad \text{where } \mathbf{q}_E = \frac{1}{M}\begin{bmatrix} \sum_{i=1}^M q_1(t_i) & \sum_{i=1}^M q_2(t_i) & \dots & \sum_{i=1}^M q_N(t_i) \\ \vdots & \vdots & \ddots & \vdots \\ \sum_{i=1}^M q_1(t_i) & \sum_{i=1}^M q_2(t_i) & \dots & \sum_{i=1}^M q_N(t_i) \end{bmatrix}. \tag{40}$$

The spatial autocorrelation matrix is then written in terms of the zero-mean time response sampling matrix as

$$\mathscr{R} = \frac{1}{M}\mathbf{q}_d^{\mathrm{T}}\mathbf{q}_d, \tag{41}$$

where $\mathscr{R}$ is, by definition, symmetric and positive semi-definite. Hence, its eigenvectors form an orthogonal basis and its eigenvalues are non-negative. In this case, the eigenvectors Ψ_j are the coherent structures or proper orthogonal modes (POMs) and the corresponding eigenvalues λ_j, or proper orthogonal values (POVs), give a measure of the mean energy contained in each mode. These are defined as

$$\mathscr{R}\Psi = \Lambda\Psi, \tag{42}$$

with

$$\Psi = [\Psi_1 \Psi_2 \ \cdots \ \Psi_N] \quad \text{and} \quad \Lambda = \mathrm{diag}(\lambda_1, \lambda_2, \dots, \lambda_N).$$

Notice that the autocorrelation matrix $\mathscr{R}$ has dimension $N \times N$. Hence, its dimension, and the number of proper orthogonal modes and values, depend only on the number of degrees of freedom and not on the time instants used for the sampling of the time response. The procedure is summarized in Fig. 8, which shows the direct method implementation algorithm of the Karhunen–Loève decomposition used here.

The time response sampling matrix $\mathbf{q}$ may then be reconstructed, in a truncated basis, by expressing $\mathbf{q}$ in terms of its time average matrix $\mathbf{q}_E$ and a reduced number K of evaluated POMs as

$$\mathbf{q} = \sum_{j=1}^{K} A_j \Psi_j^{\mathrm{T}} + \mathbf{q}_E, \tag{43}$$

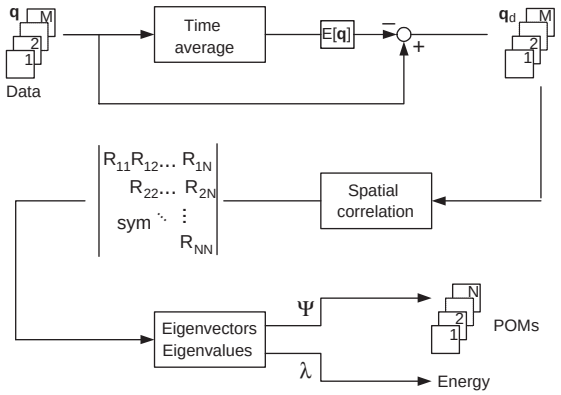

Fig. 8. Direct method implementation algorithm of KL decomposition.

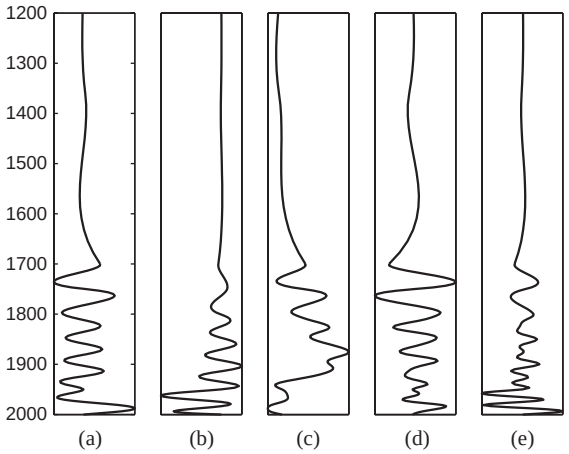

Fig. 9. Deflection in the first five proper orthogonal modes evaluated from the response. (a) $\lambda_1 = 0.55$, (b) $\lambda_2 = 0.34$, (c) $\lambda_3 = 0.03$, (d) $\lambda_4 = 0.02$, (e) $\lambda_5 = 0.05$.

where the vectors of time coefficients A_j are easily found by projecting the time response onto each POM Ψ_j, that is,

$$A_j = \mathbf{q}\Psi_j. \tag{44}$$

Notice that, by definition, the POVs also respect the following relation with the time coefficients

$$\lambda_j = \frac{1}{M}\sum_{i=1}^{M} A_j^{\mathrm{T}} A_j. \tag{45}$$

Next, this procedure is applied to the drillstring dynamics response resulting from the integration of the equations of motion (37). Moreover, one expects to obtain additional information through analysis of the POMs and POVs. These are also used to construct an optimal basis, with minimum dimension, that allows us to project the equations of motion and obtain a reduced order model, well representing the main features of the response.

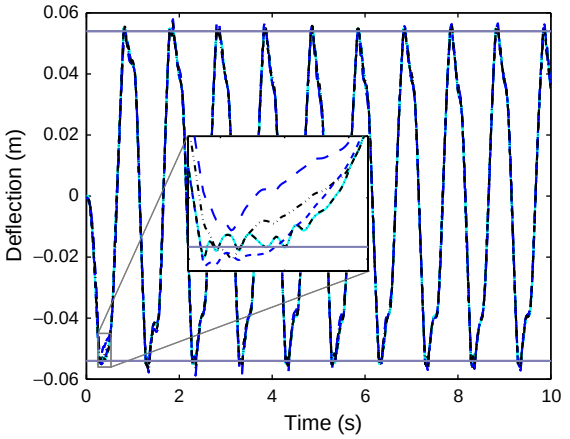

Fig. 10. Reconstruction of the transversal displacement response using the first five, nine, 15 and 30 proper orthogonal modes: — full; – –, five;-·-·-, nine; - -, 15;-··-··-, 30.

Fig. 9 shows the transversal displacement in the first five POMs evaluated from the drillstring dynamics response $\mathbf{q}$, zoomed in the drillstring bottom portion, and the corresponding POVs λ_j. It is worthwhile noting that the POVs where normalized so their sum is unitary. One may observe then that most of the energy (89%) is contained in the first two POMs and that only the bottom portion of the drillstring presents transversal deflections. This is clearly due to the fact that the upper portion of the drillstring is under traction and thus is much stiffer in bending than the bottom portion that is under compression.

Although the first five POMs are responsible for 97% of the response, one should not be able to obtain a perfect reconstruction by considering only these five modes. Indeed, it is generally recommended to consider a number of modes sufficient to sum 99.9% of the response energy. In order to analyze the quality of the reconstruction using the obtained POMs, Fig. 10 shows the reconstruction of the transversal displacement response using the first five, nine, 15 and 30 proper orthogonal modes. The percentage of the energy contained in these first POMs are respectively, 96.6567%, 99.1286%, 99.8613% and 99.9918%. Thus, one should need a little more than 15 modes to reconstruct the response, although even in this case there would be a great reduction of the model dimension, since the full FE model contains 87 degrees of freedom. Nevertheless, one could also use other measures to quantify the quality of the reconstruction. Indeed, from Fig. 10, one may observe that the overall behavior of the transversal displacement is captured even with only five POMs, the effect of bottom-hole impact being the main source of error. Another measure of the reconstruction quality was then considered, consisting of the time average of the relative error modulus between the reconstructed response v_R and the response of the full model $v_F, e = \sum_{j=1}^{M} |1 - v_F^j/v_R^j|/M$. Using this measure, one may see that using only the first five POMs leads to a reconstruction within 14% response error. This error drops to 8%, 3% and less than 1% when using the first nine, 15 and 30 POMs respectively. In the zoomed window present in Fig. 10, one may observe that there is a clear improvement of the reconstruction of the response, near the impact region, when the number of POMs is increased. In fact, when using the first 30 POMs one may capture precisely all the micro-impacts observed in the response. Nevertheless, although using only the first 15 POMs leads to small differences in the response inside the impact region,

one may observe that the main micro-impacts effects are accounted for since this reconstructed response follows almost exactly the full model response just after the impact. This means that this reconstruction, within a 3% error, may be reasonably accurate to consider only the first 15 POMs in the reduced order model.

3.3. KL reduced order model results

In this section, the equations of motion (36) are projected onto a reduced basis formed by the first 15 POMs evaluated previously. This is done through the substitution of $\bar{\mathbf{q}}(t)$ in Eq. (36) by its approximation in terms of the known truncated POMs matrix $\tilde{\Psi}$ and mean value $E[\mathbf{q}(t)]$, given as

$$\bar{\mathbf{q}}(t) = \mathbf{q}(t) - \mathbf{q}_s \approx \tilde{\Psi}\alpha(t) + E[\mathbf{q}(t)] - \mathbf{q}_s, \tag{46}$$

followed by the pre-multiplication of the resulting equation by Ψ^{T}, leading to the reduced order equations of motion

$$\mathbf{M}_\Psi \ddot{\alpha} + [\mathbf{K}_{e\Psi} + \mathbf{K}_{g\Psi}(\alpha)]\alpha = \mathbf{F}_{c\Psi} + \mathbf{F}_{p\Psi} - \mathbf{F}_{k\Psi}, \tag{47}$$

where

$$\mathbf{M}_\Psi = \tilde{\Psi}^{\mathrm{T}}\mathbf{M}\tilde{\Psi}, \quad \mathbf{K}_{e\Psi} = \tilde{\Psi}^{\mathrm{T}}\mathbf{K}_e\tilde{\Psi}, \quad \mathbf{K}_{g\Psi}(\alpha) = \tilde{\Psi}^{\mathrm{T}}\mathbf{K}_g(\mathbf{q})\tilde{\Psi},$$
$$\mathbf{F}_{c\Psi} = \tilde{\Psi}^{\mathrm{T}}\mathbf{F}_c, \quad \mathbf{F}_{p\Psi} = \tilde{\Psi}^{\mathrm{T}}\mathbf{F}_p, \quad \mathbf{F}_{k\Psi} = \tilde{\Psi}^{\mathrm{T}}[\mathbf{K}_e + \mathbf{K}_g(\mathbf{q})](E[\mathbf{q}(t)] - \mathbf{q}_s).$$

Notice that the reduced matrices and vectors of this new system have a reduced dimension of 15, which is the number of POMs considered. This system can then be solved numerically for the vector of POMs coefficients $\alpha(t)$, subject to the initial conditions $\alpha(0)$ and $\dot{\alpha}(0)$, which are meant to approximate the static initial deformed configuration $\bar{\mathbf{q}}(0) = \dot{\bar{\mathbf{q}}}(0) = \mathbf{0}$, or $\mathbf{q}(0) = \mathbf{q}_s$ and $\dot{\mathbf{q}}(0) = \mathbf{0}$.

The reduced order system was then used to simulate parametric disturbances in the impact force spring constant and sinusoidal perturbation moment frequency values. These were varied in the ranges $k = [10^7, 5 \times 10^8]$ N/m and $\omega = [4, 8]$ rad/s, respectively. Notice that the POMs were evaluated from the time response of the full order system, with given values for these two parameters $k = 10^8$ N/m and $\omega = 2\pi$ rad/s. Hence, the response of the KL reduced order system, with different values for these parameters, is expected to be only an approximation of the "correct" full order system response, since the KL modes change when the system parameters or the forcing conditions are changed. Nevertheless, the KL modes will be significantly different only when the parameters variation is large. Hence, hopefully, the original KL modes will be able to approximate the new system response.

Variation of the excitation frequency has a large effect on the time response, mainly because it induces a change in the duration of impact. This effect can be observed in Fig. 11(a), which shows the deflection at 6.25 m from the drill bit ($x = 1993.75$ m). One can see that there is a good agreement between the deflections evaluated with full order and KL reduced models. However, one can also see in Fig. 11(b) that the reduced model approximation for the axial displacement is not as good. This may be explained by the fact axial displacements, relative to the static ones, are small compared to transversal displacements and thus the first POMs are meant to represent mainly the latter.

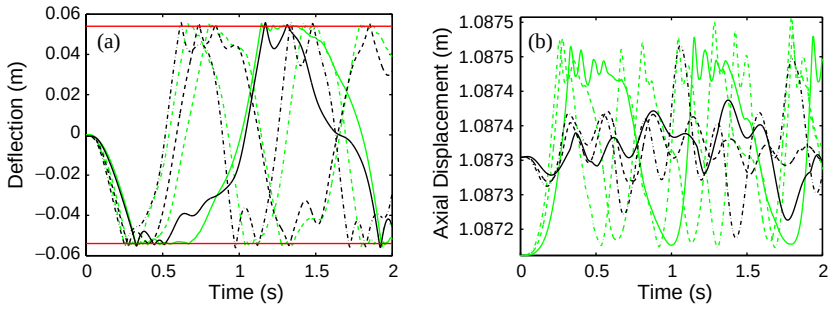

Fig. 11. (a) Transversal and (b) axial displacements evaluated with full order model (light lines) and KL reduced model (dark lines) for three values of perturbation moment frequency: —, $\omega_1 = 4$ rad/s; - -, $\omega_2 = 6$ rad/s; ---, $\omega_3 = 8$ rad/s.

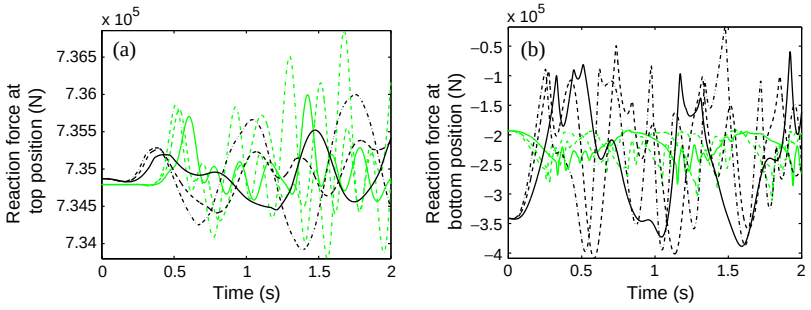

Fig. 12. Reaction forces at (a) the top and (b) bottom positions evaluated with full order model (light lines) and KL reduced model (dark lines) for three values of perturbation moment frequency: —, $\omega_1 = 4$ rad/s; - -, $\omega_2 = 6$ rad/s; ---, $\omega_3 = 8$ rad/s.

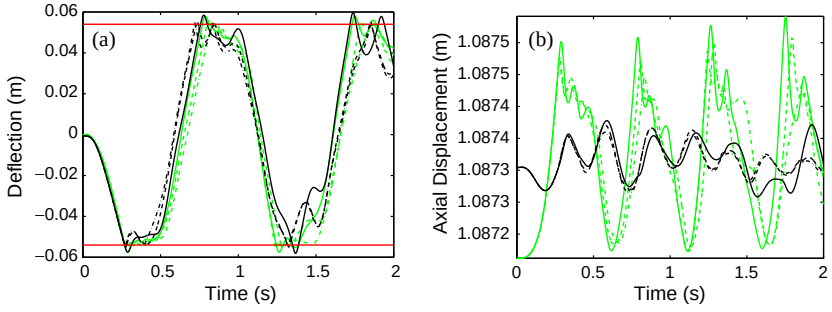

Fig. 13. (a) Transversal and (b) axial displacements evaluated with full order model (light lines) and KL reduced model (dark lines) for three values of impact force spring constant: —, $k_1 = 10^7$ N/m; - -, $k_2 = 10^8$ N/m; ---, $k_3 = 5 \times 10^8$ N/m.

Unfortunately, axial displacements are quite important to the evaluation of the reaction forces at the top and bottom positions. That is why these reaction forces are not well represented by the KL reduced order model, with only 15 POMs, as shown in Figs. 12(a) and (b).

The following figures show the effect of varying the impact force spring constant on the time response. The decrease of this parameter leads mainly to a higher penetration of the drillstring in

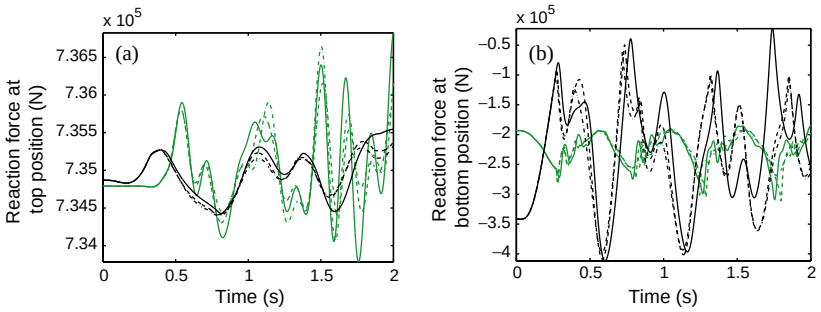

Fig. 14. Reaction forces at (a) the top and (b) bottom positions evaluated with full order model (light lines) and KL reduced model (dark lines) for three values of impact force spring constant: —, $k_1 = 10^7$ N/m, - -, $k_2 = 10^8$ N/m; -·-, $k_3 = 5 \times 10^8$ N/m.

the borehole wall. This effect may be observed in Fig. 13(a), which shows also a good agreement between the deflections evaluated by the full order and reduced order models. However, as also observed for the excitation frequency variation, here the reduced order model is unable to capture the behavior of axial displacements.

As noted also in the previous case, the KL reduced order model would require a larger number of POMs to yield a good approximation to the axial displacements and, thus, to the reaction forces at the top and bottom positions. This conclusion also holds for the variation of the impact force spring constant, as shown in Figs. 14(a) and (b).

4. Conclusions

The non-linear oscillations of a non-rotating drillstring, represented here by a vertical slender cylinder, clamped in its upper extreme, pinned in its lower one and constrained inside an outer cylinder in its lower portion, were studied in the present work. The drillstring was supposed as being subject to distributed axial loads, due to its own weight, leading to geometric softening of its lower portion and, thus, to a large number of vibroimpacts with the borehole wall. It was shown that one should account for the axial displacement dynamics, using non-linear strain–displacement relations, since the coupling of axial–bending dynamics may be very important in the dynamical behavior of general slender beams such as a drillstring. In particular, the micro-impacts, accompanying the bottom portion–hole impacts and mainly due to the beam compressive softening, are well represented only when using a non-linear axial–bending coupling. Moreover, the use of standard linear beam models may yield false predictions of the reaction forces at the top and bottom positions of the drillstring, that is the forces at the rotary table and at the formation.

Furthermore, the Karhunen–Loève decomposition was applied to the simulated dynamics of this particular system in order to obtain additional information on the system through analysis of the POMs and POVs and also to construct an optimal reduced order model. The results for the case treated here have shown that at least 15 POMs are required to reconstruct the dynamics of the impacting drillstring under a 3% error margin. These results are encouraging if one compares the dimension of the reduction basis (15 modes) with that of the original FE model (87 degrees of

freedom). A reduced order model was then developed, through projection of the FE equations of motion onto the first 15 POMs, and applied to the simulation of the dynamical response of the drillstring under variation of the impact force spring constant and excitation frequency. The results show that the KL reduced order model is capable of well representing the drillstring deflections in all cases considered. However, in order to represent the axial displacements as well, one should consider using more POMs in the projection or magnifying the axial displacements before evaluating the POMs. Future works are being directed to the improvement of these results through alternative techniques for evaluating and selecting the POMs. In addition, a three-dimensional analysis of the drillstring is also being considered through the use of a geometrically exact model proposed by Rochinha and Sampaio [18] together with a singularity-free rotation representation [19].

Acknowledgements

The authors gratefully acknowledge the financial support of "Fundação Carlos Chagas Filho de Amparo à Pesquisa do Estado do Rio de Janeiro" (FAPERJ), through grants nos. 172.038/00, 151.188/00 and 150.687/00.

References

[1] I. Sharf, Geometric stiffening in multibody dynamics formulations, *Journal of Guidance, Control, and Dynamics* 18 (4) (1995) 882–890.
[2] J. Simo, L. Vu-Quoc, The role of non-linear theories in transient dynamic analysis of flexible structures, *Journal of Sound and Vibration* 119 (3) (1987) 487–508.
[3] T.R. Kane, R.R. Ryan, A.K. Banerjee, Dynamics of a cantilever beam attached to a moving base, *Journal of Guidance, Control, and Dynamics* 10 (2) (1987) 139–151.
[4] A.K. Banerjee, J.M. Dickens, Dynamics of an arbitrary flexible body in large rotation and translation, *Journal of Guidance, Control, and Dynamics* 13 (2) (1990) 221–227.
[5] O. Wallrapp, R. Schwertassek, Representation of geometric stiffening in multibody system simulation, *International Journal for Numerical Methods in Engineering* 32 (8) (1991) 1833–1850.
[6] J. Urruzola, J.T. Celigueta, J.G. De Jalon, Generalization of foreshortening through new reduced geometrically nonlinear structural formulation, *Journal of Guidance, Control, and Dynamics* 23 (4) (2000) 673–682.
[7] M.A. Trindade, R. Sampaio, Dynamics of beams undergoing large rotations accounting for arbitrary axial deformation, *Journal of Guidance, Control, and Dynamics* 25 (4) (2002) 634–643.
[8] L. Sirovich, Turbulence and the dynamics of coherent structures, Part I: coherent structures, *Quarterly of Applied Mathematics* 45 (3) (1987) 561–571.
[9] M.F.A. Azeez, A.F. Vakakis, Proper orthogonal decomposition (POD) of a class of vibroimpact oscillations, *Journal of Sound and Vibration* 240 (5) (2001) 859–889.
[10] A. Steindl, H. Troger, Methods for dimension reduction and their application in nonlinear dynamics, *International Journal of Solids and Structures* 38 (10–13) (2001) 2131–2147.
[11] C. Wolter, R. Sampaio, Karhunen–Loève bases: applications to solid mechanics, in: *Proceedings of the First Brazilian Workshop in Applications of Dynamics and Control*, ABCM/SBMAC; São Carlos, Brazil, 2001, pp. 129–172.
[12] M.I. Friswell, J.E.T. Penny, S.D. Garvey, The application of the IRS and balanced realization methods to obtain reduced models of structures with local non-linearities, *Journal of Sound and Vibration* 196 (4) (1996) 453–468.

[13] A.S. Yigit, A.P. Christoforou, Coupled axial and transverse vibrations of oilwell drillstrings, *Journal of Sound and Vibration* 195 (4) (1996) 617–627.
[14] A.S. Yigit, A.P. Christoforou, Coupled torsional and bending vibrations of drillstrings subject to impact with friction, *Journal of Sound and Vibration* 215 (1) (1998) 167–181.
[15] R.W. Tucker, C. Wang, An integrated model for drill-string dynamics, *Journal of Sound and Vibration* 224 (1) (1999) 123–165.
[16] G.P.G. Sotomayor, J.C. Plàcido, J.C. Cunha, Drill string vibration: how to identify and suppress, in: *Proceedings of Fifth Latin American and Caribbean Petroleum Engineering Conference and Exhibition*, Rio de Janeiro, Brazil, 1997, p. SPE#39002.
[17] C. Wolter, M.A. Trindade, R. Sampaio, Obtaining mode shapes through the Karhunen–Loève expansion for distributed-parameter linear systems, *Shock and Vibration* 9 (4–5) (2002) 177–192.
[18] F.A. Rochinha, R. Sampaio, A consistent approach to treat the dynamics of flexible systems, *Journal of the Brazilian Society of Mechanical Sciences* 19 (1997) 228–241.
[19] M.A. Trindade, R. Sampaio, On the numerical integration of rigid body nonlinear dynamics in presence of parameters singularities, *Journal of the Brazilian Society of Mechanical Sciences* 23 (1) (2001) 49–62.